We are IntechOpen, the world's leading publisher of Open Access books Built by scientists, for scientists

4,800
Open access books available

122,000
International authors and editors

135M
Downloads

Our authors are among the

154
Countries delivered to

TOP 1%
most cited scientists

12.2%
Contributors from top 500 universities

CLARIVATE ANALYTICS BOOK CITATION INDEX INDEXED

WEB OF SCIENCE™

Selection of our books indexed in the Book Citation Index in Web of Science™ Core Collection (BKCI)

Interested in publishing with us?
Contact book.department@intechopen.com

Numbers displayed above are based on latest data collected.
For more information visit www.intechopen.com

23

Beating Difraction Limit using Dark States

Hebin Li[1] and Yuri Rostovtsev[2]
[1]*Department of Physics, Texas A&M University,College Station, TX 77843-4242*
[2]*Department of Physics, University of North Texas,1155 Union Circle #311427, Denton, TX 76203-5017*
USA

1. Introduction

For most three centuries after Hooke introduced optical microscopy, refinement of the instrumentation made microscopes more convinient than anything else. As in modern microscopy, a light source, an objective lens, and an eyepiece were used to project an image magnified from a 100-fold to 1,000-fold into a human eye. This range of magnifications and resolution (of the order of 200 nm) has brought cellular morphology and tissue structure into view and made optical microscopy the perfect partner for biological investigations.

A resolution constraint in optical imaging is imposed by the diffraction limit discovered by Lord Rayleigh in the 19th century. Fundamentally, this restricts the ability to resolve two distant point sources, such as stars or planets, with an angular resolution α smaller than the wavelength of light λ divided by the numerical aperture of the imaging system D, $\alpha > \lambda / D$.

The ability to create small images is important for material processing technology and for improving the resolution of microscopy for bio-medical applications [1]. In recent years, there has been a continuous effort to achieve feature sizes smaller than the diffraction limit. One method uses nonlinearity in photoresist processing to generate narrower features (involving a combination of near field and high exposure techniques). Several other methods have been presented that are able to overcome the diffraction limit of the imaging system. Quantum microscopy is based on using a nonclassical optical field approach [2, 3]. Microscopy with classical fields can be enhanced by the nonlinear optical response of the medium [4]. Classical field amplitude and phase arrangements can be used to locate the position of an atom with subwavelength precision in an atomic beam [5, 6, 7], in a cavity [8], and then to apply localization technique to lithography [9, 10, 11], and to achieve subwavelength diffraction and imaging with classical light using the Doppleron-type resonances [12, 13]. Beating diffraction limit was experimentally demonstarted [14] using the dark states.

Another method uses entangled two-photon states to write features of minimum size $\lambda / 4$ in an N-photon absorbing substrate [4,5]. There are technical difficulties associated with the implementation of all these methods, in particular the latter method requires multi-photon absorbing photoresists that are insensitive to single photon effects which is difficult to achieve.

An early discovery in the modern field of quantum optics is that by going to higher-order correlations in the radiation field, one can improve resolution in stellar interferometers, vis a

Source: Advances in Lasers and Electro Optics, Book edited by: Nelson Costa and Adolfo Cartaxo,
ISBN 978-953-307-088-9, pp. 838, April 2010, INTECH, Croatia, downloaded from SCIYO.COM

vis the Hanbury Brown-Twiss effect. Photon correlation interferometry is a powerful tool with applications ranging from the macro- to the micro-cosmos. For example, to measure stellar diameters and resolve binary stars the Hanbury Brown-Twiss effect can be used. As is also known that it is possible to improve the resolution of optical microscopy [2,3,4] by using photon correlation interferometry and entangled quantum states. This has been demonstrated in the elegant experiment [25] via two photon down conversion.

Below we show how to improve microscopy by using higher order quantum correlation function, namely, $G^{(2)}$. Very recently, this concept has been brought down to the microscopic realm and carried the science an important step further by introducing a novel two-photon source, composed of Raman emission pairs, which allow the two-photon correlation to extract source details with a resolution that is far better than that allowed by the Rayleigh criterion [1].

Not long time ago, it has been shown that applying the geometry and physics of the original Raman quantum eraser scheme [2] allows one to resolve molecular markers separated by distances smaller than the wavelength of the probing radiation. Note that in many biophysical studies, the shape or conformation of a protein or a DNA strand is monitored as a function of various parameters. One way of making such measurements involves attaching markers, such as dye molecules or quantum dots, to two known points on the protein and observing their fluorescence as they move apart.

The key features that enable the improved resolution in this scheme is the entanglement in the quantum field and the carefully chosen geometry of the photodetection apparatus, as described below. The space-time correlations between the emitted photons have novel interference properties that show anti-bunching and bunching effects spaced apart by the Rabi period. Experiments analyzing the photon statistics of this scheme [2,3] hint at new methods for the coherent storage and coupling of quantum information between atomic and photonic systems.

In this Chapter, we review physics background of the methods and techniques that allow researchers to beat the so-called diffraction limit using classical as well as quantum fields. In particularly, we review the possibility of creating spatial patterns having subwavelength size by using the so-called dark states formed by the interaction between atoms and optical fields. These optical fields have a specified spatial distribution. Our experiments in Rb vapor display spatial patterns that are smaller than the length determined by the diffraction limit of the optical system used in the experiment. This approach may have applications to interference lithography and might be used in coherent Raman spectroscopy to create patterns with subwavelength spatial resolution.

2. Beating diffraction limit with classical fields

2.1 Two-level atoms

Let us show here how the idea works for two-level atoms. The Hamiltonian of a two-level atom interacting with an optical resonant field (see Fig. 1) is given by

$$H = \hbar\Omega_d |a\rangle\langle b| + adj., \tag{1}$$

where $\Omega_d = \wp_d E_d / \hbar$ is the Rabi frequency of the drive E_d field; $\wp_d$ is the dipole moment of the atomic transitions. Then, the atomic response is given by the set of density matrix equations [17]

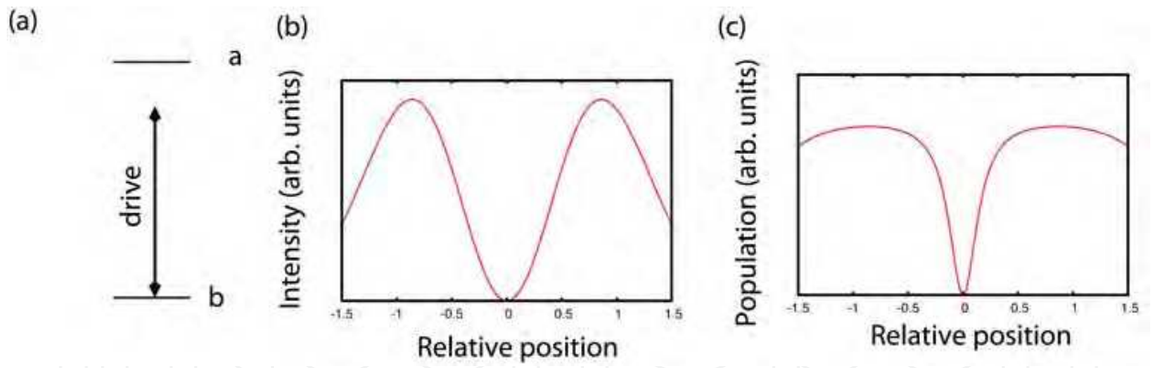

Fig. 1. (a) Energy diagram of a two-level system interacting with a strong drive field. (b) Distribution of the drive field intensity vs. a transverse spatial coordinate. (c) Dependence of the population excited in the atomic medium vs spatial position.

$$\dot{\rho} = -\frac{i}{\hbar}[H,\rho] - \frac{\Gamma\rho + \rho\Gamma}{2} \tag{2}$$

where Γ describes the relaxation processes. In particular for a two-level system the set of equation has the following form

$$\dot{\rho}_{ab} = -\Gamma_{ab}\rho_{ab} + i\Omega_d(n_a - n_b), \tag{3}$$

$$\dot{n}_a = -\gamma n_a + i\Omega_d(\rho_{ab} - \rho_{ba}), \tag{4}$$

where $n_a = \rho_{aa}$, $n_b = \rho_{bb}$; $\Gamma_{ab} = \gamma_{ab} + i(\omega_{ab} - \nu)$, $\gamma_{ab} = 1/T_2$, $\gamma = 1/T_1$ (T_1 and T_2 are corresponding longitudinal and transverse relaxation times). Solving Eqs.(3,4) in a steady-state regime, we obtain

$$\rho_{ab} = i\frac{n_a - n_b}{\Gamma_{ab}}\Omega_d, \tag{5}$$

$$n_a = \frac{2Re\left(\frac{|\Omega_d|^2}{\Gamma_{ab}}\right)}{\gamma + 2Re\left(\frac{|\Omega_d|^2}{\Gamma_{ab}}\right)} n_b \tag{6}$$

Then the population in the upper atomic level is given by

$$n_a = \frac{2Re\left(\frac{|\Omega_d|^2}{\Gamma_{ab}}\right)}{\gamma + 4Re\left(\frac{|\Omega_d|^2}{\Gamma_{ab}}\right)}, \tag{7}$$

for the case of resonance, $\nu = \omega_{ab}$, it is reduced to

$$n_a = \frac{2|\Omega|^2 T_1 T_2}{1 + 4|\Omega|^2 T_1 T_2}. \tag{8}$$

We now assume that the drive field has a spatial distribution of intensity.

$$|\Omega|^2 = |\Omega_0|^2 f(x), \tag{9}$$

where $f(x)$ is the spatial distribution of the intensity of optical drive field. For example, in the case of interference of two waves with wavevectors k_1 and k_2, the optical field is

$$E_d = E_1 e^{ik_1 r} + E_2 e^{ik_2 r}, \tag{10}$$

and intensity distribution is given by

$$|E_d|^2 = |E_1|^2 + |E_2|^2 + 2E_1 E_2 \cos(k_1 - k_2)r = (|E_1| - |E_2|)^2 + 4|E_1||E_2| \sin^2 2(k_1 - k_2)r, \tag{11}$$

intensity at different spatial position changes between $(|E_1| - |E_2|)^2$ and $(|E_1| + |E_2|)^2$. Introducing $G = 2|\Omega_0|^2 T_1 T_2$, we can write

$$\rho_{aa} = \frac{Gf(x)}{1 + 2Gf(x)}. \tag{12}$$

Then, for the drive field at the position being near to its zero the Rabi frequency is given by

$$|\Omega_d(z,x)|^2 = |\Omega_0|^2 \left(\frac{x}{L}\right)^2, x \ll L, \tag{13}$$

where $\Omega_0 = \Omega_d(z,x_0)$, L is the separation distance between the peaks of the drive field distribution (for interference patern, $L = \lambda / 2\sin(\theta / 2) > \lambda / 2$). A typical excitation profile vs. x shown in Fig. 1(c) demonstrates that the spatial width of excitation can be smaller than the intensity distribution of the optical field, and even smaller than the spot size determined by diffraction limited size. Indeed, the width of spatial distribution of excited atoms is given by

$$\Delta x \simeq \frac{L}{2\sqrt{G}} = \frac{L}{2\Omega_0 \sqrt{T_1 T_2}}. \tag{14}$$

The most important feature of Eq.(14)is that the width depends on the relaxation parameters and the field strength, but not the diffraction of optical field.

2.2 Using Stark shifts

Three-level atoms provide more flexibility for the localization of the excited atoms or molecules because of different physical mechanisms can be involved. For example, it is shown in Fig. 2 how to use Stark shifts for atomic localization [5]. Level structure of a three-level atom is shown in Fig. 2a (for example ^{152}Sm). Geometry of atomic beam and optical beams can be seen in Fig. 2b. Probe 1 beam is used to optically pump all population in level c. Then atoms reach the region where they have inhomogenious drive beam which is detuned from the atomic resonance and simultaneously this region has a probe beam 2 with frequency ν_2. Due to Stark shift atoms at different spatial location have energy of the excited state a as

$$e_{\pm} = \frac{\Delta}{2} \pm \sqrt{\left(\frac{\Delta}{2}\right)^2 + |\Omega|^2}, \tag{15}$$

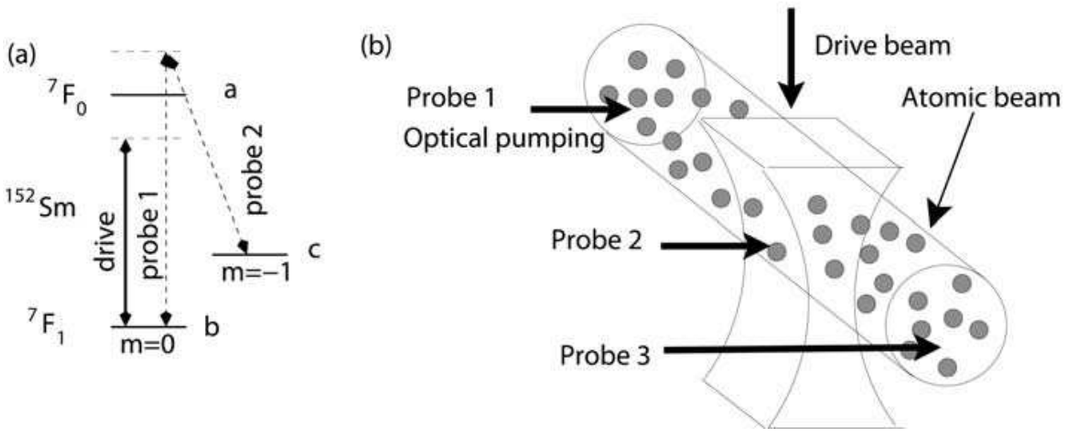

Fig. 2. Qualitative description of the idea of using Stark shifts for atomic localization. (a) Level structure of ^{152}Sm, as an example, and the applied fields. (b) Geometry of atomic beam of ^{152}Sm and optical beams. Probe 1 beam is used to pump all population in level *c*. Drive beam detuned from the atomic resonance and it has spatial distribution such that, at each location it has different Stark shift. Probe 2 beam resonantely interacts with atoms at the particular spatial location where it is resonant to the optical transition. The effect of probe 2 beam is pumping resonant atoms to level *b*. Probe 3 is the field to excite fluorescence from the atoms in the ground state *b*.

where Δ is the detuning of the drive beam, and Ω is the Rabi frequency of the drive beam. The atoms have different detuning from the resonance at different positions, and some of them are at the resonance when the detuning is less than the spontaneous emission rate γ,

$$e_+ - \nu_2 + \frac{1}{\Delta}\frac{\partial|\Omega_0|^2}{\partial x}\Delta x \le \gamma. \tag{16}$$

The resonant interaction of these atoms with probe 2 beam results in population of the ground state *b*. Then, the probe 3 beam resonantely interacts with atoms at the particular spatial location where it is resonant to the optical transition to cause fluorescence which is detected. The localization of the atoms can be found from Eq.(16)

$$\Delta x = \frac{\gamma\Delta}{\frac{\partial|\Omega_0|^2}{\partial x}}, \tag{17}$$

which is also determined by the relaxation rate γ, detuning Δ, and the spatial derivative of drive field intensity, and, the most important is not directly related to the diffraction, and consequently can be smaller than the wavelength of optical radiation as was demonstrated in [5].

2.3 Beating diffraction limit by using Dark states

The Hamiltonian of a three-level atom interacting with optical fields (see the inset in Fig. 4) is given by

$$H = \hbar\Omega_d|a\rangle\langle b| + \hbar\Omega_p|a\rangle\langle c| + adj., \tag{18}$$

where $\Omega_{d,p} = \wp_{d,p} E_{d,p} / \hbar$ are the Rabi frequencies of the drive E_d and the probe E_p fields, respectively; $\wp_{d,p}$ are the dipole moments of the corresponding optical transitions. Then, the atomic response is given by the set of density matrix equations [17]

$$\dot{\rho} = -\frac{i}{\hbar}[H, \rho] - \frac{\Gamma\rho + \rho\Gamma}{2} \tag{19}$$

where Γ describes the relaxation processes.
Here, we present a new approach that is based on coherent population trapping [15, 16, 17, 18, 19]. Optical fields applied to a three-level quantum system excite the so-called *dark state*, which is decoupled from the fields. Similar approaches using coherent population trapping have also been developed by several groups (for example, see [20, 22, 23, 24]).

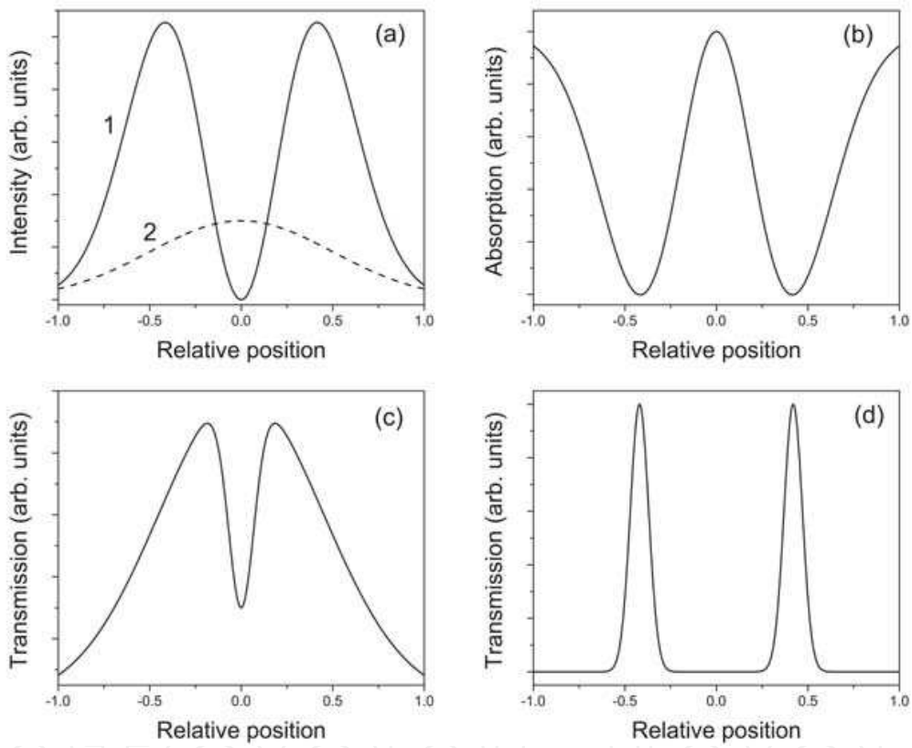

Fig. 3. Qualitative description of the idea. (a) Distribution of the drive (1) and the probe (2) fields vs. a transverse spatial coordinate at the entrance to the cell. (b) Dependence of the absorption coefficient given by Eq.(21) vs position. Plots (c) and (d) show the distribution of the probe beam after propagating through the cell. Case (c) is for a strong drive field and relatively low optical density. Case (d) is for a relatively weak drive field and large optical density.

As a qualitative introduction, assume that the drive field Rabi frequency Ω_d has the particular spatial distribution sketched in Fig. 3(a) by the solid line (1). The weak probe field Rabi frequency Ω_p ($\Omega_p \ll \Omega_d$) has a diffraction limited distribution (shown by the dashed line (2) in Fig. 3(a)). The probe and drive fields are applied to the atom (see the inset in Fig. 4, for the case of ^{87}Rb atoms, where $|a\rangle = |5^2P_{1/2}, F = 1, m = 0\rangle$, $|b\rangle = |5^2S_{1/2}, F = 1, m = -1\rangle$, $|c\rangle = |5^2S_{1/2}, F = 1, m = +1\rangle$). At all positions of nonzero drive field, the dark state, which is given

[15, 16, 17, 18, 19] by $|D\rangle = (\Omega_p|c\rangle - \Omega_d|b\rangle)/\sqrt{\Omega_p^2+\Omega_d^2}$, is practically $|b\rangle$. When the drive field is zero, the dark state is $|c\rangle$, and the atoms at these positions are coupled to the fields and some atoms are in the upper state $|a\rangle$. The size of a spot where the atoms are excited depends on the relaxation rate γ_{cb} between levels $|b\rangle$ and $|c\rangle$. For $\gamma_{cb} = 0$, the size of spot is zero, smaller than the optical wavelength.

The propagation of the probe field Ω_p through the cell is governed by Maxwell's Equations and, for propagation in the z-direction, can be written in terms of the probe field Rabi frequency as

$$\frac{\partial \Omega_p}{\partial z} = -i\eta\rho_{ab} - i\frac{1}{2k}\frac{\partial^2}{\partial x^2}\Omega_p. \tag{20}$$

The first term accounts for the dispersion and absorption of the resonant three-level medium, and the second term describes the focusing and/or diffraction of the probe beam. The density matrix element ρ_{ab} is related to the probe field absorption which in turn depends on the detuning and the drive field. This is characterized by an absorption coefficient:

$$\kappa = \eta\frac{\Gamma_{cb}}{\Gamma_{ab}\Gamma_{cb} + |\Omega_d(z,x)|^2}, \tag{21}$$

where $\Gamma_{cb} = \gamma_{cb} + i\omega$ and $\Gamma_{ab} = \gamma + i\omega$; $\omega = \omega_{ab} - \nu$ is the detuning from the atomic frequency ω_{ab}; γ is the relaxation rate at the optical transition; and $\eta = 3\lambda^2 N\gamma_r/8\pi$; N is the atomic density; γ_r is the spontaneous emission rate. We now assume that the drive field has a distribution of intensity near its extrema given by

$$|\Omega_d(z,x)|^2 = |\Omega_0|^2\begin{cases}\left[1-\left(\frac{x-x_0}{L}\right)^2\right], & x \simeq x_0,\\ \left(\frac{x}{L}\right)^2, & x \ll L,\end{cases} \tag{22}$$

where $\Omega_0 = \Omega_d(z,x_0)$, L is the separation distance between the peaks of the drive field distribution, and a typical absorption profile vs. x is shown in Fig. 3(b). Neglecting the diffraction term in Eq.(20), we can write an approximate solution for Eq. (20) as

$$\Omega_p(z,x) = \Omega_p(z=0,x)\exp(-\kappa z). \tag{23}$$

For relatively low optical density ($\kappa z \simeq 1$), nearly all of the probe field propagates through the cell except for a small part where the drive field is zero (see Fig. 3(a)). Absorption occurs there because the probe beam excites the atomic medium. The width of the region of the excited medium, in the vicinity of zero drive field, is characterized by

$$\Delta x = L\sqrt{\frac{\Gamma_{ab}\Gamma_{cb}}{|\Omega|^2}}, \tag{24}$$

where $\Omega = \Omega_d(z = 0, x = 0)$. This region is small, but its contrast is limited because of the finite absorption of the medium at the center of optical line (Fig. 3(c)).

For higher optical density, this narrow feature becomes broadened (compare Fig. 3(c) and (d)), but two narrow peaks are formed during the propagation of the probe beam (see Fig. 3(d)). For zero detuning, their width is given by

$$\Delta x = L\sqrt{\frac{|\Omega|^2}{\eta\gamma_{cb}z}}. \tag{25}$$

The drive field provides flexibility for creating patterns with sizes smaller than the wavelength of the laser. The distribution of fields is governed by electrodynamics and has a diffraction limit, while the distribution of molecules in their excited states is NOT related to the diffraction limit, but rather determined by the relaxation rates Γ_{ab} and Γ_{cb}, and thus can have spatial sizes smaller than the wavelength.

3. Experimental demonstration

In this section, we report a proof-of-principle experiment in Rb vapor to demonstrate our approach. We have observed that the distribution of the transmitted probe beam intensity has a double-peak pattern, which is similar to that of the drive beam, but the width of the peaks of the probe beam is narrower than that of the drive beam.

The experimental schematic is shown in Fig. 4. We obtain a good quality spatial profile by sending the radiation of an external cavity diode laser through a polarization-preserving single-mode optical fiber. The laser beam is vertically polarized and split into two beams (drive and probe). The probe beam carries a small portion of the laser intensity, and its polarization is rotated to be horizontal.

To create a double-peak spatial distribution for the drive field, the drive beam is split into two beams that cross at a small angle, using a Mach-Zehnder interferometer (shown in the dashed square of Fig. 4). A typical two-peak interference pattern of crossing beams is shown as Fig. 4A.

The probe and drive beams combine on a polarizing beam splitter, arranged so that the probe field and the interference pattern of the drive field are overlapped in a Rb cell. The Rb cell has a length of 4 cm, and is filled with ^{87}Rb. A magnetic shield is used to isolate the cell from any environmental magnetic fields, while a solenoid provides an adjustable, longitude magnetic field. The cell is installed in an oven that heats the cell to reach an atomic density of 10^{12} cm^{-3}. The laser is tuned to the D_1 line of ^{87}Rb at the transition $5^2S_{1/2}(F = 2) \rightarrow 5^2P_{1/2}$ ($F = 1$).

As stated above, the probe and drive beams have the orthogonal linear polarizations. A quarter-wave plate converts them into left and right circularly polarized beams, which couple two Zeeman sublevels of the lower level and one sublevel of the excited level of the Rb atoms (see the inset of Fig. 4).

After passing through the cell, the probe and drive beams are converted back to linear polarizations by another quarter-wave plate and the separated by a polarizing beam splitter (PBS). The power of transmitted probe field is monitored by a photodiode (PD). The spatial intensity distribution of probe field is recorded by an imaging system, consisting of the lens L3 and a CCD camera.

The intensity of the probe beam is low enough that its transmission through the cell is almost zero without the presence of drive laser. Applying the drive laser makes the atomic medium transparent for the probe laser wherever the EIT condition is satisfied. If the drive laser has a certain transverse spatial distribution, then that pattern can be projected to the transmission profile of the probe laser.

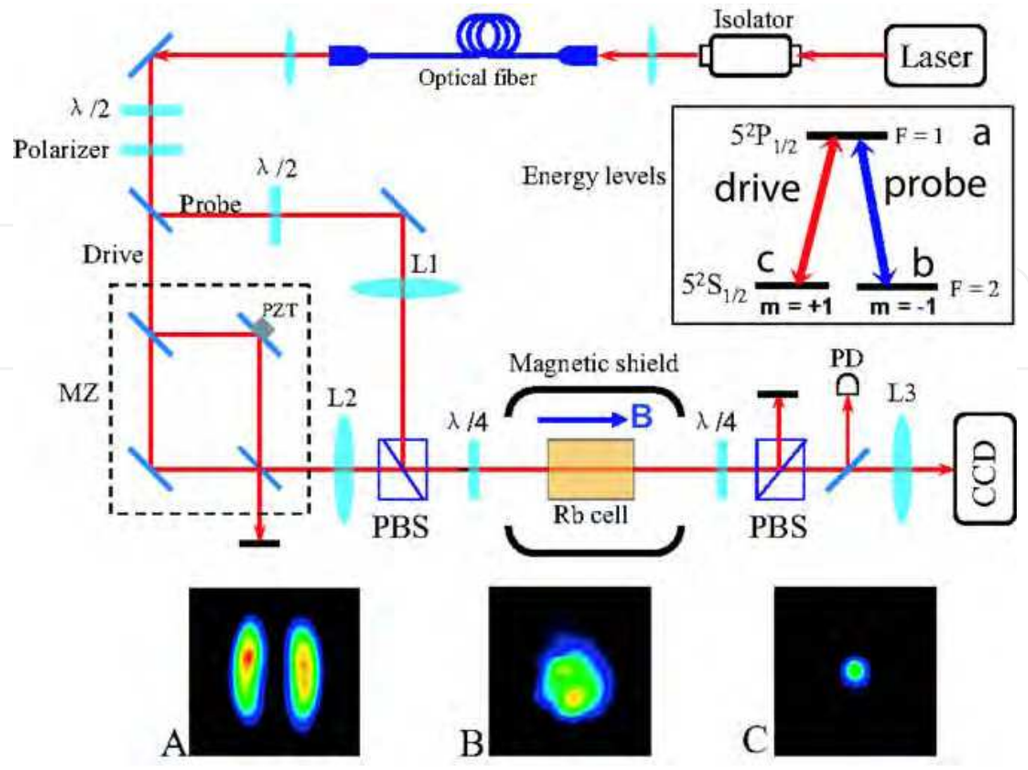

Fig. 4. Experimental schematic. λ /2: half-wave plate; λ /4: quarter-wave plate; L1, L2, L3: lenses; MZ: Mach-Zehnder interferometer; PZT: piezoelectric transducer; PBS: polarizing beam splitter, PD: photo diode; CCD: CCD camera. Picture A is the spatial intensity distribution of the drive field. Picture B is the beam profile of the parallel probe beam without the lens L1. Picture C is the beam profile of the diffraction limited probe beam with the lens L1. All three of pictures have been made with with the camera at the location of the cell, which has temporally been removed. The inset is the energy diagram of the Rb atom, showing representative sublevels.

Two different experiments have been performed. In the first experiment, the lenses L1 and L2 are not used, and the probe beam is a parallel beam with a diameter of 1.4 mm. The image of the drive intensity distribution in the cell is shown in Fig. 5(a). The probe intensity has a Gaussian distribution before entering the cell, and its distribution is similar to the drive intensity distribution after the cell. As shown in Fig. 5(b), however, the transmitted probe intensity has a distribution that has sharper peaks compared with the pattern of the drive intensity. The horizontal cross-sections of the drive and the transmitted probe distributions are shown in Figs. 5(c) and (d) respectively. In the drive intensity profile, the width (FWHM) of the peaks is 0.4 mm. The width (FWHM) of the peaks in the transmitted probe intensity profile is 0.1 mm. The spacing between two peaks is the same for both the drive and transmitted probe fields. We define the *finesse* as the ratio of the spacing between peaks to the width of peaks. The finesse of the transmitted probe intensity distribution is a factor of 4 smaller than that of the drive intensity distribution.

In the second experiment, the lenses L1 and L2 are used. A parallel probe beam (Fig. 4B) with a diameter of 1.4 mm is focused by the lens L1, which has a focal length of 750 mm. The beam size at the waist is 0.5 mm, which is diffraction limited. To assure experimentally that

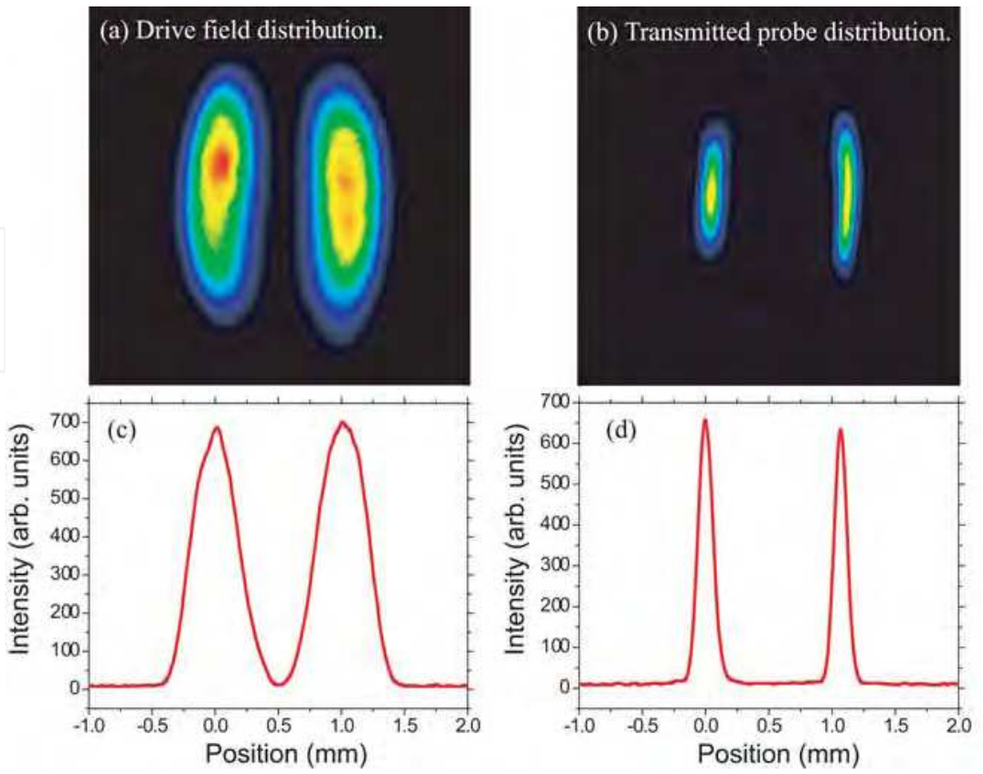

Fig. 5. The results of the experiment with a parallel probe beam. Picture (a) shows the image of the intensity distribution of the drive field in the Rb cell. Picture (b) shows the intensity distribution of the transmitted probe field. Curves (c) and (d) are the corresponding intensity profiles. The widths of the peaks in curves (c) and (d) are 0.4 mm and 0.1 mm, respectively.

the beam is diffraction limited, we increased the beam diameter of the parallel beam by the factor of 2, and the beam size at the waist became two times smaller. The lens L2 is used to make the drive beam smaller in the Rb cell, where the pattern of drive field is spatially overlapped with the waist of the probe beam. Classically, there should be no structures at the waist of the probe beam because it is diffraction limited. Structures can be created in a region smaller than the diffraction limit in our experiment, however. The experimental result is shown in Fig. 6. The drive field still has a double peak intensity distribution (Fig. 6(a)). The transmission of the diffraction limited probe beam also has a double-peak intensity distribution as shown in Fig. 6(b). Curves (c) and (d) are the beam profiles of the drive and transmitted probe beams respectively. The width of the peaks in the drive beam is 165 μm, and the width of the peaks in the transmitted probe beam is 93 μm. The finesse of the transmitted probe beam is 1.8 times greater than that of the drive beam. For the probe beam, the structure created within the diffraction limit has a size characterized by the width of peaks (93 μm). This characteristic size is 5 times smaller than the size of the diffraction limited probe beam (500 μm, see the spot of Fig. 4(C)).

At the end, we would like to stress here that the concept based on dark states successfully works in Rb vapor. One can see that the width of the probe image (C) is at least three times smaller than the width of the drive image (A). Although the diffraction limit is "beaten," the experiment does not violate any laws of optics. The probe beam is diffraction limited, but

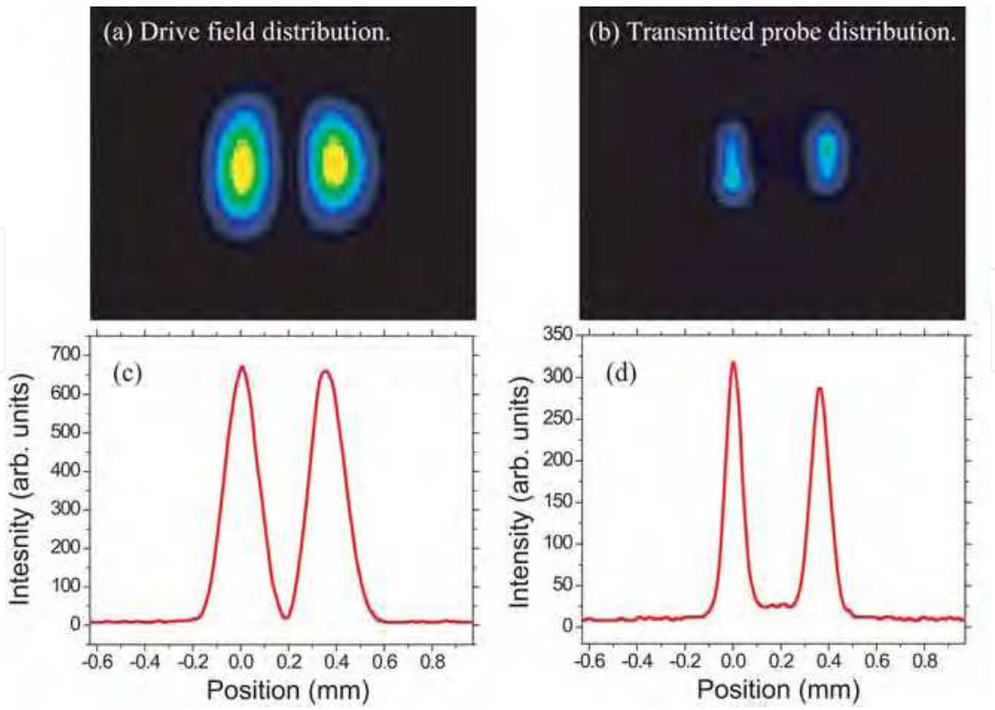

Fig. 6. The results of the experiment with the diffraction limited probe beam. Picture (a) shows the image of the intensity distribution of the drive field in the Rb cell. Picture (b) shows the image of the intensity distribution of the transmitted probe field. Curves (c) and (d) are the corresponding profiles. The widths of the peaks in curves (c) and (d) are 165 μm and 93 μm, respectively.

the atoms are much smaller than the size of diffraction-limited beam. Moreover, due to the strong nonlinearity of the EIT, the characteristic size of the pattern in the transmitted probe beam is much smaller than that of the drive beam and the diffraction limit of the probe beam.

We have also measured the narrowing effect vs. the detuning of the probe field and have performed simulations using the density matrix approach. The results are shown in Fig. 7. The calculations reproduce the data satisfactorily. The dependence on detuning has not been considered in [20, 23, 24, 22]. It is unique for our approach and can be understood in the following way. Absorption by the atomic medium given by Eq.(21) with a drive intensity distribution given by Eq.(22) can be written as

$$\kappa = \eta \left(\frac{\gamma_{cb}}{|\Omega|^2} + \frac{\gamma\omega^2}{|\Omega|^4} + \left(\frac{\gamma_{cb}}{|\Omega|^2} + 2\frac{\gamma\omega^2}{|\Omega|^4} \right) \left(\frac{x}{L} \right)^2 \right). \tag{26}$$

Then, ratio of the width of the probe intensity distribution to the width of the drive intensity distribution is given by

$$R = \frac{L}{\Delta x} = \sqrt{\eta z \left(\frac{\gamma_{cb}}{|\Omega|^2} + 2\frac{\gamma\omega^2}{|\Omega|^4} \right)}. \tag{27}$$

From this we see that the finesse increases with the detuning.

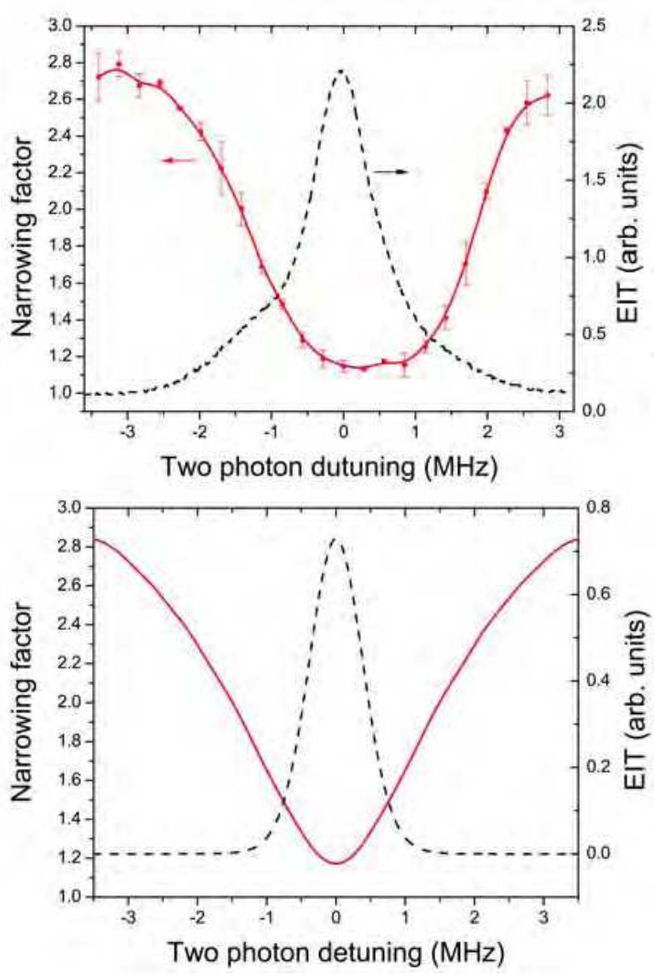

Fig. 7. Narrowing of the transmitted probe intensity distribution as function of the probe detuning: (a) experimental results and (b) theoretical simulation. The transmition of the probe is shown as well.

It is worth to mention here that a proof-of-principle experiment has been already reported in [14] that the concept works in Rb vapor and have experimentally demonstrated the possibility of creating structures having widths smaller than those determined by the diffraction limits of the optical systems. The results obtained here can be viewed as an experimental verification of our approach, as well as evidence supporting the theoretical predictions and results obtained by others [20, 23, 24, 22]. The challenges associated with pushing our method to the subwavelength regime are formidable. In vapor or gaseous medium, transit-time broadening is the dominant dephasing mechanism that limits the smallness of the region in which a dark state can be formed. Solid-state systems may be more appropriate, although, the most difficult aspect of this approach is devising a way to observe subwavelength structures. This technique might be used in microscopy by studying the distribution of molecules with subwavelength resolution or in lithography by manipulating molecules in the excited state. Also, note that it may be possible to apply this approach to coherent Raman scattering (for example, CARS). This may improve the spatial resolution of CARS microscopy.

4 Microscopy with quantum fields

4.1 Simplified model

Let us consider two identical marker molecules that are separated by distance d from each other (see Fig. 8). The level structure of molecules is shown in Fig. 9. We also assume that there is no dipole-dipole interaction between molecules, i.e. the level structure does not depend on the distance between molecules.

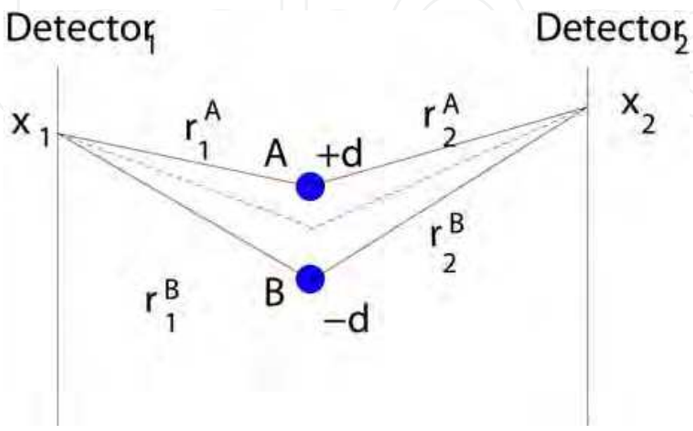

Fig. 8. Two marker molecules at some distance that can be resolved by quantum microscopy analyzing shifts or magnitudes of $G^{(2)}$ fringes.

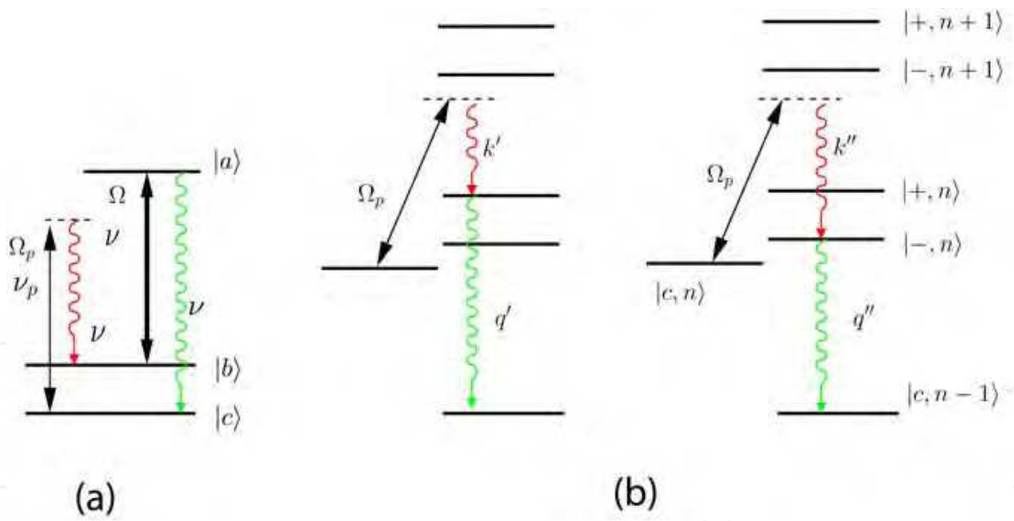

Fig. 9. (a) Raman scheme to generate correlated pair of photons is shown. (b) In dressed state basis, one can see that the system is ladder scheme with splitted intermediate state similarly to eraser scheme studied in [2].

We shine the laser radiation on the system. It consists of two fields that we treat as classical fields: the first field Ω_p is weak and it has large one-photon detuning from the resonance; the second field Ω is much stronger than the first one ($\Omega_p \ll \Omega$) and it is resonant to the electron transition between the ground state and the excited state of two marker molecules.
The first field having frequency ν_p excited the molecule from ground state level b to generate a Raman Stockes photon, and the molecule ends up in the level c. Then the second laser field

having frequency ν_d excites the molecule to level a to generate anti-Stokes photon and ends down to the starting ground level b.

Now, if the two emitted photons are well separated in time, then the two photon state $|\Psi\rangle$ can be factorized as a sum of products of one photon Stokes ($|\nu\rangle$) and anti-Stokes ($|\omega\rangle$) states from molecules at A and B, that is

$$|\Psi\rangle = \frac{1}{\sqrt{2}}[|\nu,\omega\rangle_A + |\nu,\omega\rangle_B]. \tag{28}$$

Then the spontaneous Stokes and anti-Stokes radiation of Fig. 1a will be independent, and the Glauber photon-photon correlation function factorizes. To see this we recall

$$G^{(2)}_{\nu\omega} = \left\langle \Psi \middle| \hat{E}^{(-)}(1)\hat{E}^{(-)}(2)\hat{E}^{(+)}(2)\hat{E}^{(+)}(1) \middle| \Psi \right\rangle \tag{29}$$

in which $G^{(2)}_{\nu\omega} = G^{(2)}_{\nu\omega}(1,1';2,2')$, $\hat{E}^{(+)}(1)$ is the positive frequency (annihilation operator) part of the electric field and $E^{(-)}(1)$ is the corresponding negative frequency (creation operator); 1 stands for $\tilde{\mathbf{r}}_1$, t_1 where $\tilde{\mathbf{r}}_1$ is the vector to detector 1, etc (Fig. 1a). The times t_i are controlled by e.g., shutters.

The two-photon probability $G^{(2)}(1,2) = |\Psi(1,2)|^2$ for a single molecule has been calculated in [2]. The photon-photon correlation function for two molecules has been calculated from the two photon amplitude [2], and it is given by

$$\begin{aligned} G^{(2)}/\mathscr{C} = {} & e^{-\Gamma\tau_1}e^{-\gamma\tau_{21}}\sin^2\tilde{\Omega}\tau_{21} + e^{-\Gamma\tau_1'}e^{-\gamma\tau_{21}'}\sin^2\tilde{\Omega}\tau_{21}' + \\ & e^{-(\Gamma/2)(\tau_1+\tau_1')}e^{-(\gamma/2)(\tau_{21}+\tau_{21}')}\sin\tilde{\Omega}\tau_{21}\sin\tilde{\Omega}\tau_{21}' \times \\ & 2\cos[\nu(\tau_1-\tau_1') + \omega(\tau_2-\tau_2')] \end{aligned} \tag{30}$$

with $\tau_1' > 0, \tau_1 > 0, \tau_2 > \tau_1$ and $\tau_2' > \tau_1'$. Physically, this describes the finite time, governed by $\tilde{\Omega}$, to promote the molecule from b to a (similarly to the driven two-level system, see [17]). Mathematically, the vanishing of $G^{(2)}$ when $\tau_1 = \tau_2$, is a result of quantum interference between the two paths of Fig. 2.

4.2 Determine minimal distance between marker molecules

We are interested to determine how small distance between molecules d can be. To answer this question we present $G^{(2)}$ as series on d. The geometry is shown in Fig. 8. The distance from molecule A to detector 1 is given by

$$r^{A,B}_{1,2} = \sqrt{d^2_{1,2} + (x_{1,2} \mp d/2)^2} \simeq R_{1,2} \mp \frac{dx_{1,2}}{2R_{1,2}}, \tag{31}$$

We can rewrite $\tilde{\Omega}\,\tau_{21}$ as $\frac{\tilde{\Omega}}{c}r_{12} = \alpha - d\beta$, and $\tilde{\Omega}\tau_{21}'$ as $\frac{\tilde{\Omega}}{c}r_{12} = \alpha + d\beta$, where $\alpha = k_\Omega(R_1 - R_2) = k_\Omega R_{12}$ and $\beta = (\frac{x_1}{2R_1} - \frac{x_2}{2R_2})$. Interference term is given by $\cos[\nu(\tau_1 - \tau_1')+\omega(\tau_2 - \tau_2')] = \cos\xi\, d$, where $\xi = k[\frac{x_1}{R_1} + \frac{x_2}{R_2}]$.

The $G^{(2)}(x_1,x_2)$ is given then by

$$G^{(2)}(x_1,x_2)=\sin^2(\alpha-d\beta)+\sin^2(\alpha+d\beta)+2\sin(\alpha-d\beta)\sin(\alpha+d\beta)\cos\xi d. \quad (32)$$

First, we consider moving two detectors together, $x_1 = x_2$, so

$$G^{(2)}(x_1)=\sin^2[\tilde{k}_\Omega(R_1-D)]\cos^2[\tilde{k}d\frac{x_1}{R_1}] \quad (33)$$

where we introduce $\tilde{k}_\Omega = \frac{\tilde{\Omega}}{c}(n_1-n_2)$, $\tilde{k} = k(n_1+n_2)$. The location of the fringes is given by $\frac{\partial G^{(2)}(x_1)}{\partial x_1}=0$, or

$$\frac{D^2}{R_1^2}\frac{\tilde{k}d}{x_1}\tan[\tilde{k}d\frac{x_1}{R_1}]\tan[\tilde{k}_\Omega(R_1-D)]=\tilde{k}_\Omega. \quad (34)$$

Using $kd \ll 1$, the position of the first fringe can be given by

$$x_p=\sqrt{(\frac{\pi}{2\tilde{k}_\Omega}+D)^2-D^2}-\frac{\tilde{k}^2d^2D^2}{\tilde{k}_\Omega^2(\frac{\pi}{2\tilde{k}_\Omega}+D)^2\sqrt{(\frac{\pi}{2\tilde{k}_\Omega}+D)^2-D^2}}. \quad (35)$$

Minimal distance between molecules can be found at the given accuracy of measurement of fringe position as

$$d_{min}=\frac{\tilde{k}_\Omega(\frac{\pi}{2\tilde{k}_\Omega}+D)\sqrt{(\frac{\pi}{2\tilde{k}_\Omega}+D)^2-D^2}}{\tilde{k}D}\sqrt{\varepsilon}, \quad (36)$$

where $\varepsilon = \delta x_p/x_p$. While the change of distance between molecules can be measured much more accurately, namely

$$\delta d_{min}=\frac{\lambda}{8\pi^2(n_1+n_2)^2}\left(\frac{\lambda}{d}\right)F(\tilde{k}_\Omega,D)\varepsilon, \quad (37)$$

where we introduce a function

$$F(\tilde{k}_\Omega,D)=\frac{\pi\tilde{k}_\Omega D}{2}\left(\frac{\pi}{2\tilde{k}_\Omega D}+2\right)\left(\frac{\pi}{2\tilde{k}_\Omega D}+1\right)^2 \quad (38)$$

optimizing the Rabi frequency of the drive laser field we obtain

$$\delta d_{min}=\frac{\lambda}{8\pi^2(n_1+n_2)^2}\left(\frac{\lambda}{d}\right)\frac{3\sqrt{5}+7}{\sqrt{5}-1}\varepsilon \quad (39)$$

for $\tilde{k}_\Omega D = \pi/(\sqrt{5}-1)$. Thus optimize driving field we obtain

$$\delta d=\frac{\lambda}{3(n_1+n_2)^2}\left(\frac{\lambda}{d}\right)\varepsilon \quad (40)$$

Second, In the limit of small $d \ll r_{1,2}, R_{1,2}, d_{1,2}, |x_{1,2}|$, we can rewrite Eq.(32) as

$$G^{(2)}(x_1,x_2) \simeq (4-\xi^2 d^2)\sin^2\alpha \tag{41}$$

Then the ratio is given by

$$\frac{G^{(2)}(x_1)}{G^{(2)}(x_1')} = \frac{\sin^2\alpha(x_1)}{\sin^2\alpha(x_1')}\left(1-\frac{\xi^2(x_1)-\xi^2(x_1')}{4}d^2\right) \tag{42}$$

Assume that $x_1+x_2 = 0$ we obtain

$$\frac{G^{(2)}(x_1)}{G^{(2)}(x_1')} = \frac{\sin^2\alpha(x_1)}{\sin^2\alpha(x_1')}\left(1+\frac{\xi^2(x_1')}{4}d^2\right) \tag{43}$$

In addition, assume that we can measure the ratio with $\varepsilon = 1\%$ accuracy

$$\frac{\xi^2(x_1')}{4}d^2 \simeq 10^{-2} \rightarrow d_{min} = \frac{\sqrt{2}}{\pi}\frac{\lambda}{2}\sqrt{\frac{R_1}{x_1}}\sqrt{\varepsilon} \simeq \frac{\lambda}{20\pi}. \tag{44}$$

Interesting feature of the microscope is that it has high sensitivity to small changing of the distance between molecules. Indeed,

$$\delta d = \frac{\lambda}{2\pi^2(n_1+n_2)^2}\left(\frac{R_1}{x_1}\right)^2\left(\frac{\lambda}{d}\right)\varepsilon. \tag{45}$$

5. Final remarks

We have reviewed the basic physics underlying to localize atoms and molecules better than the the so-called diffraction limit. Precise atomic position measurement has attracted a great deal of interest for many years because of many applications such as atom lithography, microscopy, and atom localization. On the other hand, the resonance fluorescence emitted collectively by many interacting two-level atoms in an external driving laser field has been studied extensively for different parameter ranges [26, 27, 28, 29, 30, 31, 32, 33]. Following the idea of reaching subwavelength resolution for nonidentical, individually addressable objects [15], a relation between collective fluorescent light and the geometry of the setup was also shown experimentally [34].

In [35], motivated by the localization of an atom inside an optical field [36], it has been showed that distance and position information can be obtained by measuring the fluorescence spectrum of a two-atom system inside a standing-wave field, relying entirely on far-field measurement techniques. Typically, this scheme will be limited by the difficulties in fixing the positions of the two atoms rather than by constraints of the measurement scheme itself, which in principle allows one to achieve resolution far below the classical Rayleigh limit of optical microscopy technology.

In addition to the fluorescence spectrum, also the intensity-intensity correlation function of the light emitted by a collection of two- and three-level atom systems subject to driving fields has been investigated [31, 32, 37, 38, 39]. Most of these works, however, focused on nonclassical properties of the emitted field.

The role of the dipole-dipole interaction between atoms has been recently taken into account in [21]. In particular, it was demonstrated how the distance information can be obtained by measuring the intensity-intensity correlation function of the emitted fluorescence field. It turns out that the power spectrum of the intensity-intensity correlation function is well suited to gaining distance information over a wide range of parameters with high accuracy. The obtained results can be applied to physical systems which may be approximated as two-level systems, where the two energy states are connected by an electric-dipole-allowed transition. Possible examples include atoms, molecules, and artificial quantum systems such as quantum dots.

6. Acknowledgement

We gratefully acknowledge the support of the Office of Naval Research, the Robert A. Welch Foundation (Grants # A1261 and A1547), and the CRDF (Award No. AZP-3123-BA-08 of Azerbaijan National Science Foundation).

7. References

[1] C.A. Mack, Fundamental Principles of Optical Lithography : the Science of Microfabrication, (Chichester,West Sussex, England:Wiley, 2007).
[2] M.O. Scully, K. Druhl, Phys. Rev. A25, 2208 (1982);U. Rathe,M.O. Scully, Lett.Math. Phys. 34, 297 (1995);M.O. Scully, U. Rathe, C. Su, G.S. Agarwal, Opt. Commun. 136, 297 (1997).
[3] A. N. Boto, P. Kok, D. S. Abrams, S. L. Braunstein, C. P. Williams, and J. P. Dowling, Phys. Rev. Lett. 85, 2733-2736 (2000).
[4] V. Westphal and S.W. Hell, Phys. Rev. Lett. 94, 143903 (2005). S.W. Hell and J. Wichmann, Opt. Lett. 19, 780 (1994)M. Dyba and S.W. Hell, PRL 88, 163901 (2002)
[5] J. R. Gardner,M. L. Marable, G. R. Welch, and J. E. Thomas, Phys. Rev. Lett. 70, 3404 (1993).
[6] K. D. Stokes, C. Schnurr, J. R. Gardner, M. Marable, G. R. Welch, and J. E. Thomas, Phys. Rev. Lett. 67, 1997 (1991).
[7] J. E. Thomas, Opt. Lett. 14, 1186 (1989). J. E. Thomas, Phys. Rev. A 42, 5652 (1990); K. D. Stokes, C. Schnurr, J. R. Gardner, M. Marable, G. R. Welch and J. E. Thomas, Phys. Rev. Lett. 67, 1997 (1991).
[8] J.-T. Chang, J. Evers, M.O. Scully and M.S. Zubairy, Phys. Rev. A 73, 031803(R) (2006); J.-T. Chang, J. Evers, and M.S. Zubairy, Phys. Rev. A 74, 043820 (2006).
[9] A.P. Chu, K.K. Berggren, K.S. Johnson, M.G. Prentiss, Quant. Semclas. Opt. 8, 521 (1996).
[10] K.S. Johnson, J.H. Thywissen, N.H. Dekker, K.K. Berggren, A.P. Chu, R. Younkin, M.G. Prentiss, Science 280, 1583 (1998).
[11] J.H. Thywissen, M.G. Prentiss, New J. Phys. 7, 47 (2005).
[12] S. Qamar, S.Y. Zhu,M.S. Zubairy, Phys. Rev. A61, 063806 (2000);M. Sahrai, H. Tajalli, K.T. Kapale, M.S. Zubairy, Phys. Rev. A72, 013820 (2005).
[13] P. R. Hemmer, A. Muthukrishnan,M. O. Scully, and M. S. Zubairy, Phys. Rev. Lett. 96, 163603 (2006); Q. Sun, P.R. Hemmer, M.S. Zubairy, Phys. Rev. A75, 065803 (2007).
[14] H. Li, V.A. Sautenkov,M.M. Kash, et al., Phys. Rev. A78, 013803 (2008).
[15] S. E. Harris, Phys. Today 50, 36 (1997).

[16] E. Arimondo, in *Progress in Optics* edited by E. Wolf, Vol. XXXV, p.257 (Elsevier Science, Amsterdam, 1996).
[17] M. O. Scully and M. S. Zubairy, Quantum Optics (Cambridge University Press, Cambridge, UK, 1997).
[18] J. P. Marangos, J. Mod. Opt. 45, 471 (1998).
[19] M. Fleischhauer, A. Imamoglu, J.P. Marangos, Rev. Mod. Phys. 77, 633 (2005).
[20] M. Kiffner, J. Evers, and M. S. Zubairy, Phys. Rev. Lett. 100, 073602 (2008).
[21] J.T. Chang, J. Evers, M. S. Zubairy, Phys. Rev. A74, 043820 (2006).
[22] G.S. Agarwal, K.T. Kapale, J. Phys. B 39, 3437 (2006).
[23] A.V. Gorshkov, L. Jiang, M. Greiner, P. Zoller, M.D. Lukin, Phys. Rev. Lett. 100, 093005 (2008).
[24] D. D. Yavuz, N. A. Proite, Phys. Rev. A 76, 041802 (2007).
[25] M. DAngelo,M.V. Chekhova, and Y. Shih, PRL 87, 013602 (2001).
[26] G. S. Agarwal, A. C. Brown, L. M. Narducci, and G. Vetri, Phys. Rev. A 15, 1613 (1977).
[27] A. S. Jahangir Amin and J. G. Cordes, Phys. Rev. A 18, 1298 (1978).
[28] G. Lenz and P. Meystre, Phys. Rev. A 48, 3365 (1993).
[29] T. Richter, Opt. Acta 30, 1769 (1983).
[30] H. S. Freedhoff, Phys. Rev. A 19, 1132 (1979); R. D. Griffin and S. M. Harris, ibid. 25, 1528 (1982).
[31] Z. Ficek, R. Tanas, and S. Kielich, Opt. Acta 30, 713 (1983).
[32] Z. Ficek and R. Tanas, Phys. Rep. 372, 369 (2002).
[33] M. Macovei and C. H. Keitel, Phys. Rev. Lett. 91, 123601 (2003).
[34] C. Hettich, C. Schmitt, J. Zitzmann, S. Kuhn, I. Gerhardt, and V. Sandoghdar, Science 298, 385 (2002).
[35] J.-T. Chang, J. Evers, M. O. Scully, and M. S. Zubairy, Phys. Rev. A 73, 031803(R) (2006).
[36] T. Azim, M. Ikram, and M. S. Zubairy, J. Opt. B: Quantum Semiclassical Opt. 6, 248 (2004); F. Ghafoor, S. Qamar, and M. S. Zubairy, Phys. Rev. A 65, 043819 (2002); S. Qamar, S.-Y. Zhu, and M. S. Zubairy, ibid. 61, 063806 (2000); F. Le Kien, G. Rempe, W. P. Schleich, and M. S. Zubairy, ibid. 56, 2972 (1997); M. Sahrai, H. Tajalli, K. T. Kapale, and M. S. Zubairy, ibid. 72, 013820 (2005).
[37] G. C. Hegerfeldt and D. Seidel, J. Opt. B: Quantum Semiclassical Opt. 4, 245 (2002).
[38] C. Skornia, J. von Zanthier, G. S. Agarwal, E.Werner, and H.Walther, Phys. Rev. A 64, 063801 (2001).
[39] M. O. Scully and C. H. Raymond Ooi, J. Opt. B: Quantum Semiclassical Opt. 6, S575 (2004).

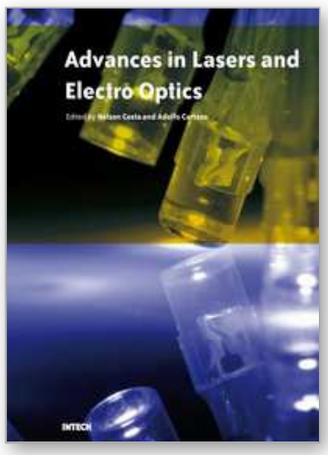

Advances in Lasers and Electro Optics

Edited by Nelson Costa and Adolfo Cartaxo

ISBN 978-953-307-088-9
Hard cover, 838 pages
Publisher InTech
Published online 01, April, 2010
Published in print edition April, 2010

Lasers and electro-optics is a field of research leading to constant breakthroughs. Indeed, tremendous advances have occurred in optical components and systems since the invention of laser in the late 50s, with applications in almost every imaginable field of science including control, astronomy, medicine, communications, measurements, etc. If we focus on lasers, for example, we find applications in quite different areas. We find lasers, for instance, in industry, emitting power level of several tens of kilowatts for welding and cutting; in medical applications, emitting power levels from few milliwatt to tens of Watt for various types of surgeries; and in optical fibre telecommunication systems, emitting power levels of the order of one milliwatt. This book is divided in four sections. The book presents several physical effects and properties of materials used in lasers and electro-optics in the first chapter and, in the three remaining chapters, applications of lasers and electro-optics in three different areas are presented.

InTech Europe
University Campus STeP Ri
Slavka Krautzeka 83/A
51000 Rijeka, Croatia
Phone: +385 (51) 770 447
Fax: +385 (51) 686 166
www.intechopen.com

InTech China
Unit 405, Office Block, Hotel Equatorial Shanghai
No.65, Yan An Road (West), Shanghai, 200040, China
中国上海市延安西路65号上海国际贵都大饭店办公楼405单元
Phone: +86-21-62489820
Fax: +86-21-62489821

IntechOpen